



Large gains in leaf scale photosynthetic rates of sparsely vegetated arid and semi-arid lands



Jiabin Pu¹✉, Yuhe Chang¹, Alexander J. Winkler², Zhenpeng Zuo¹, Chi Chen¹,
Yuri Knyazikhin¹ & Ranga B. Myneni¹

Photosynthesis drives carbon into terrestrial ecosystems via gross primary production (GPP), rising $\sim 3\%$ decade $^{-1}$ globally, paralleled by green leaf area expansion. Both trends stem from CO₂ fertilization (CFE), climate change, and landcover change, yet spatial mismatches exist between GPP and leaf area changes. Canopy scale GPP changes are separated into those resulting from leaf area changes and those from changing photosynthetic rates per unit leaf area. The latter, by normalizing for leaf area, isolate production dependency on CO₂, light and water availability, and the kinetics of the process itself. Arid/semi-arid shrublands and grasslands show substantial CO₂ assimilation gains, dominated by CFE and beneficial climate effects. Conversely, croplands and forests exhibit declining leaf assimilation rate due to increased shading from excessive greening and adverse climate shifts (e.g., reduced precipitation, higher VPD). The Sudano-Sahelian zone exemplifies assimilation increases in sparse vegetation, while conspicuously greening regions like China and India face assimilation declines. This pattern of canopy GPP increases from gains in both leaf scale assimilation rates and leaf area in sparse vegetation of inhospitable climates, and only from leaf area gains in more productive vegetation of favorable environments, whilst counter-intuitive, suggests an unforeseen potential for carbon sequestration in sparsely vegetated lands.

Terrestrial gross primary production refers to photosynthetic carbon fixation by vegetation canopies (GPP_C in g C m $^{-2}$ ground area time $^{-1}$)¹. This flux, marking the entry point for carbon into the terrestrial system, is currently increasing at $\sim 3\%$ decade $^{-1}$ globally^{2,3}. The green leaf area, over which photosynthesis happens, defined as one-sided green leaf area per unit ground area in broadleaf vegetation and one-half the total needle surface per unit ground area in needleleaf vegetation⁴, is also increasing at the same rate⁵⁻⁷. Several key factors contribute to these changes in GPP_C and leaf area. The CO₂ fertilization effect (CFE), some aspects of climate change (e.g., warming in the North), nitrogen deposition, land use and land cover changes are evidently the principal reasons for these GPP_C and leaf area index (LAI) changes^{2,3,8-14}. The impact of elevated atmospheric CO₂ on vegetation manifests through two primary mechanisms: (1) a biochemical effect: the CO₂ fertilization effect (CFE), which enhances photosynthesis and biomass accumulation, thereby altering canopy structure²; (2) a radiative effect: increased CO₂ concentration leads to warming and climate change, while also modifying the light condition and nitrogen availability, all of which affect the vegetation photosynthesis¹⁵. However, not all climate

change impacts are positive, particularly in arid and semi-arid regions, climate change negatively affects plant growth due to increased water stress^{16,17}. Furthermore, intensive human land-use practices have amplified GPP_C and LAI changes, particularly in China and India⁵.

However, spatially there is a mis-match in where and by how much GPP_C and leaf area are changing. In Amazonian rainforests, it was found that leaf area decreased but vegetation canopy productivity remained constant in the 2010 drought year^{18,19}, and that little change in leaf area was measured in contrast to substantial decreases in canopy photosynthesis in the 2015–2016 drought period²⁰. Greening in herbaceous vegetation, for example, is much less than in woody vegetation globally, GPP_C gains however are much larger in the former than the latter⁶. This decoupling is especially noticeable in arid and semi-arid regions. Satellite observations in these areas show minimal increases in leaf area due to persistent water limitations, yet these ecosystems experience disproportionately large surges in GPP_C during occasional wet periods¹⁷.

Mounting evidence suggests that light availability limits carbon fixation in two ways: directly through incident light levels and the ratio of direct

¹Department of Earth and Environment, Boston University, Boston, MA, USA. ²Max Planck Institute for Biogeochemistry, Jena, Germany. ³Department of Ecology, Evolution, and Natural Resources, Rutgers University, New Brunswick, NJ, USA. ✉e-mail: om7759@bu.edu

solar to diffuse sky radiation, and indirectly through changes in canopy structure, primarily via increased self-shading of leaves as leaf area expands^{21,22}. This constraint on light availability may explain the discrepancy between vegetation greening, *i.e.*, adding extra leaves, and GPP_C changes. Consequently, this study hypothesized that greening tends to lower the average light reaching leaves in moderate to dense vegetation. This reduction can counteract the positive effects of CO_2 fertilization (CFE), leading to smaller gains in GPP_C . Conversely, in sparse vegetation with low leaf areas, such as arid and semi-arid regions, greening does not significantly affect light levels. In these areas, the increased leaf area will reinforce the CFE effect, resulting in substantial GPP_C gains. This interaction between the CFE and light levels in vegetation has not been identified before. To understand this interaction and its implications to the carbon cycle, long-term observations and model estimates are analyzed here. Canopy scale GPP changes are separated into those resulting from leaf area changes and those from changing photosynthetic rates per unit leaf area. The latter, by normalizing for leaf area, isolate production dependency on CO_2 , light and water availability, and the kinetics of the process itself.

Estimates of GPP_C from observations and models during the 2001–2021 period and projections for the rest of this century are discussed here. The observation-based estimates are derived from a combination of solar-induced chlorophyll fluorescence measurements of the Orbiting Carbon Observatory-2 and CO_2 exchange data of flux towers (GOSIF²³). The modeled GPP_C estimates are – (*i*) an ensemble average of three Production Efficiency Models (PEMs) forced with two climate data sets, (*ii*) an ensemble average of 18 Dynamic Global Vegetation Models (DGVMs) of the TRENDY project²⁴ and (*iii*) an ensemble average of seven Earth System Models (ESMs) of the CMIP6 project²⁵ for the historical period (2001–2014) and projections to year 2100 based on three emission scenarios. Sections in Methods detail the three PEMs (\$1), the forcing climate data (\$2), parameter optimisation (\$3), validation and intercomparison with peer GPP_C products (\$§4–6), the TRENDY DGVMs (\$7) and CMIP6 ESMs (\$8). Results in Supplementary Figs. 1 to 5, and also those presented here, show that modelled GPP_C from simple PEMs compare well to those from process-based dynamic models (TRENDY and ESMs), peer GPP_C data sets^{26–28}, and observations (GOSIF and AmeriFlux). Only statistically significant (Mann-Kendall test, $P \leq 0.1$) results are discussed below.

Results and Discussion

§1 Global Mis-match Between Leaf Area Expansion and Canopy Productivity Gains

Annual means of GPP_C from PEMs and DGVMs are comparable to the GOSIF estimate (128 vs. 131 Pg C yr^{-1}). They reflect an upward trend of 3.9 to 5.2 Pg C yr^{-1} decade⁻¹ during the 2001–2021 period (Fig. 1a). The same from ESMs are 123 Pg C yr^{-1} and 3.8 Pg C yr^{-1} decade⁻¹. About 44% of the $106 \times 10^6 \text{ km}^2$ of total vegetated area displays a positive trend, most conspicuously in China, Europe, India, North America, Sahel and abutting area, and northern Siberia. Declines are observed in only 5% of the vegetated lands, prominent only in the Brazilian Amazon. The $\sim 10 \text{ Pg C}$ of total GPP_C gain is mostly from herbaceous vegetation (64%). Of note, croplands account for nearly a quarter of this gain while occupying only 11% of the total vegetated area. The more productive woody vegetation ($\sim 55\%$ of GPP_C share) contributes a third of the increase in GPP_C . Overall, the modelled patterns match well with observations (Supplementary Fig. 6a) and previous studies^{29,30}.

At the same time, there have been increases in green leaf area of vegetation^{2,6,15,31–34}. Globally, gains in leaf area and GPP_C seem comparable in magnitude (3.3 vs. 3.1 to 4.6% decade⁻¹) and extent; 44% of the vegetated lands exhibit greening, 7% browning and the rest no changes (Supplementary Fig. 7). Indeed, the same causal markers have been invoked to explain the greening and browning of lands in the satellite era^{2,6,15}. Regions exhibiting prominent greening visually correspond to those with large GPP_C increases. Numerically however, greening in herbaceous vegetation is less than that of woody vegetation (44% for herbaceous vs. 56% for woody), opposite of shares in GPP_C gains (64% for herbaceous vs. 36% for woody).

Croplands illustrate this disparity starkly, 23% share of GPP_C gain with only 15% of greening. This mis-match in rates of change between GPP_C and leaf area is delved into below.

Conceptually, the amount of photosynthate produced under prevailing conditions depends on light and dark reactions within the leaf, the availability of raw resources of light, water, nutrients and CO_2 , and the extent of photosynthesizing leaf area^{35–38}. GPP_C changes can be therefore separated into those resulting from leaf area changes and those from changing assimilation rates per unit leaf area. The latter, by normalising for leaf area, isolate production dependency to resource availability and kinetics of the process itself. This leaf scale photosynthetic rate can be calculated as $\text{GPP}_C \div \text{LAI}$; reliable LAI data are widely available^{4,7,39–42} (Methods §§9 and 10). It will be denoted from hereon as GPP_L ($\text{g C m}^{-2} \text{ leaf area day}^{-1}$). The accuracy and independence of GPP_C (Supplementary Figs. 1, 2, and 3) and LAI^{7,39,42} data used to estimate GPP_L imbue confidence in capturing the aggregate leaf scale dynamics, *i.e.*, kinetics of reactions within the leaf and utilization of light, water and CO_2 resources, in spite of the representation of vegetation canopy as one big leaf in PEMs.

The pattern of GPP_L changes (Fig. 1b) is remarkably different than the individual patterns of changes in GPP_C (Fig. 1a) and LAI (Supplementary Fig. 7b). The patterns agree well with those based on observations (Supplementary Fig. 6). At the global scale, there is little to no change in GPP_L (inset Fig. 1b) contrary to a previous report based on shorter records⁴³. However, the global numbers belie important GPP_L variations regionally^{16,43}. Leaf assimilation rates trend upward in sparsely vegetated lands in Argentina, Australia, Kazakhstan, Sahel and adjoining areas, and USA, Negative GPP_L trends are seen in the more densely vegetated areas of Brazil, sub-Arctic Canada, China, northern Europe and India. Especially China and India, which exhibit large positive trends in both GPP_C and LAI due to intensive land management practices⁵, show significant GPP_L declines. The Sahel and adjoining lands, being the only exception globally, show consistent positive trends in GPP_C , LAI^{44,45} and GPP_L , in a prominent west to east swath. The reasons for this surprising pattern of GPP_L gains in inhospitable climes and losses in favourable environments are explored below.

§2 Large Gains in Leaf Scale Photosynthetic Rates of Sparsely Vegetated Arid and Semi-Arid Lands

Studying the distributions of GPP_C , LAI and GPP_L trends reveals large gains in sparse vegetation, and these decrease with increase in growing season mean LAI (Table 1 and Fig. 2a). Sparse vegetation ($\sim \text{LAI} < 1$), most of which is shrublands and grasslands in arid and semi-arid regions (Supplementary Fig. 7c), constitutes 41% of global vegetated area and contributes 17% of GPP_C . Only in these land covers is the net change in GPP_L statistically significant, reflecting a gain of 2.4% decade⁻¹. The rest of the land covers show no changes in GPP_L , although the individual trends of GPP_C and LAI are statistically positive. There are, of course, significant local GPP_L changes at all vegetation densities (Fig. 2a), but the only net change is a gain in sparse vegetation. The results thus inform on larger increases in GPP_C relative to LAI in sparse vegetation and matching changes for the rest (Table 1), *i.e.*, GPP_C gains in vegetation with $\text{LAI} < 1$ are due to gains in both GPP_L and LAI, while in denser canopies only due to LAI. This hints at additive impacts of causal agents in sparse vegetation and opposing impacts elsewhere, as elucidated below.

The trends in GPP_L (Figs. 1b and 2a) can be unpacked into the individual effects of ambient CO_2 concentration, climate and light on leaf photosynthate production. The fertilisation effect of increasing atmospheric CO_2 concentration (CFE) on GPP_L is well known^{2,3,12,13}. The climate effect includes GPP_L dependency on temperature⁹, vapour pressure deficit⁴⁶ and soil moisture⁴⁷ via precipitation. The effect of light on GPP_L results from altered light distribution on leaves within the canopy due to changes in vegetation structure, including leaf area^{21,48}. The three effects can be quantified through specialized simulations with simple PEMs forced with corresponding observations (Methods §11).

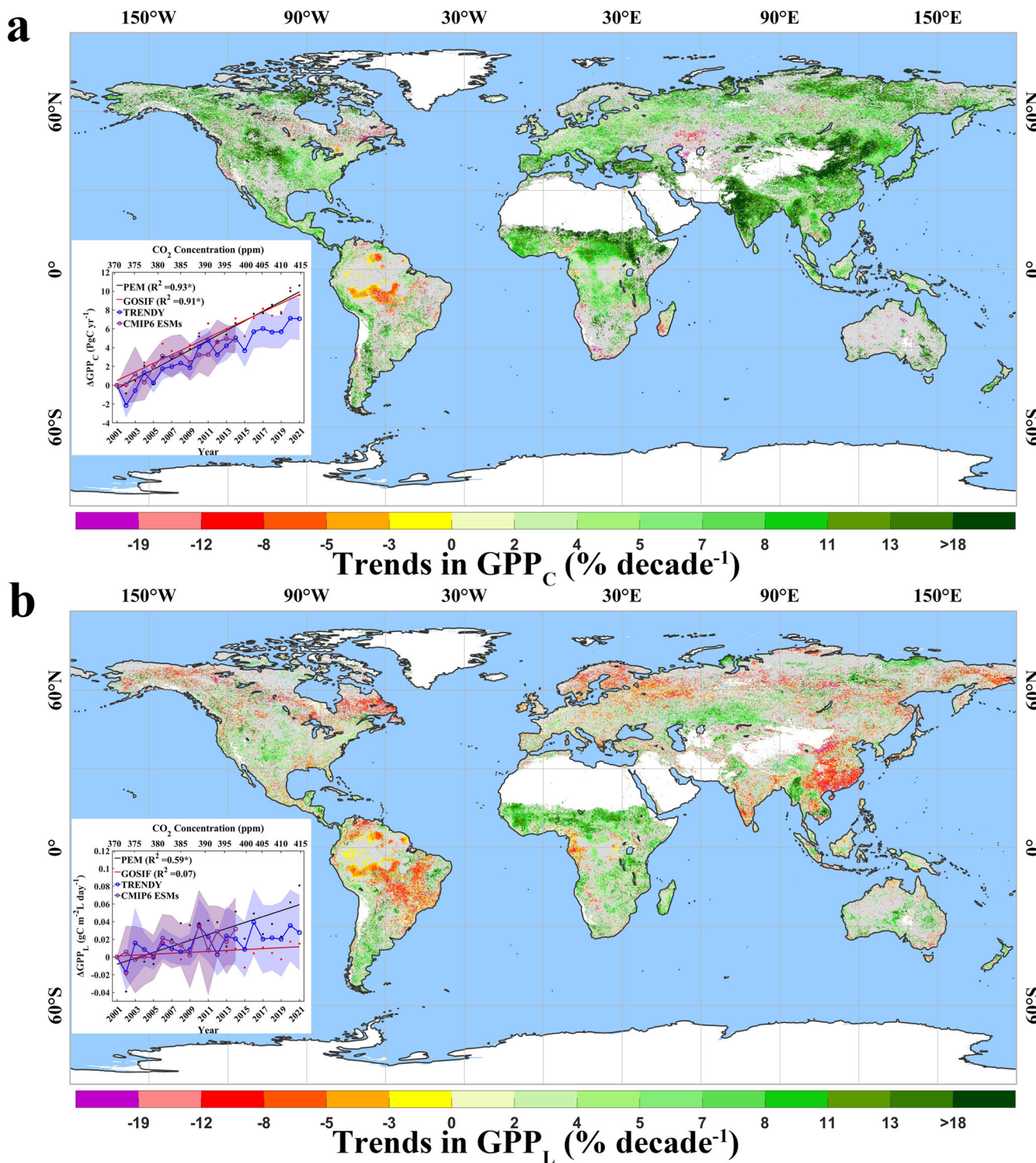


Fig. 1 | Trends in annual gross primary production at the canopy (GPP_C) and leaf (GPP_L) scales. **a** Ensemble mean GPP_C (g C m^{-2} ground area year $^{-1}$) of three Production Efficiency Models (PEMs) forced with two climate data sets (§5). **b** GPP_L is $GPP_C \div LAI$ (g C m^{-2} leaf area year $^{-1}$), where LAI is the ensemble mean of two observational data sets (§9). Only statistically significant trends are colour-coded (Mann-Kendall test, $P \leq 0.1$). The insets show global-scale trends from observations

based GOSIF data² (red line is a linear fit to yearly data shown as red dots), PEMs (black line and dots), 18 TRENDY models (mean as blue line and range as blue shading; §7) and seven CMIP6 ESMs (in green; §8). The calculation of GPP_L is described in §10. The “*” in the inserts means that the correlation of the fitted line is significant. Analogous patterns from observations are shown in Supplementary Fig. 6. Section numbers refer to sections in Methods.

The fertilisation and climate effects represent direct and indirect effects of CO_2 buildup in the atmosphere²⁴. Changes in GPP_L due only to the CFE are positive (Fig. 2b). These are large in grasses and crops ($3.7\% \text{ decade}^{-1}$) and modest in tropical forests ($2.2\% \text{ decade}^{-1}$). The bi-modality at $LAI < 2$ is due to land cover specific CFE. For example, the CFE is $2.3\% \text{ decade}^{-1}$ in

arid shrublands where the growing season average LAI is 0.7, while it is $3.7\% \text{ decade}^{-1}$ in semi-arid and dry sub-humid grasslands and croplands which have a LAI of 0.9. This general pattern of higher fertilisation effect in sparse vegetation has been observed in situ⁴⁹ and attributed to increased water use efficiency⁴⁷. Local climate effects are both positive and negative (Fig. 2c),

Table 1 | Distribution of trends in GPP_C , LAI and GPP_L in broad LAI intervals

	Vegetated Area (%)	Global GPP_C (%)	Trend in LAI ($\% \text{ decade}^{-1}$)	Trend in GPP_C ($\% \text{ decade}^{-1}$)	Trend in GPP_L ($\% \text{ decade}^{-1}$)
0.1 < LAI <= 1.0	40.90	17.15	5.33*	7.24*	2.40*
1.0 < LAI <= 2.0	31.20	30.60	4.37*	4.43*	0.30
2.0 < LAI <= 3.0	13.10	18.44	4.57*	4.26*	0.13
3.0 < LAI <= 4.0	2.92	5.62	3.31*	2.75*	-0.49
LAI > 4.0	11.88	28.19	1.10*	1.62*	0.59

LAI refers to growing season average leaf area index, where the growing season is defined as the period when canopy scale gross primary production (GPP_C) > 0 and LAI > 0.1. The leaf scale gross primary production is denoted by GPP_L . The proportions of vegetated area and GPP_C in each LAI class interval is also shown. Asterisks indicate statistically significant trends (Mann-Kendall test, $P \leq 0.1$).

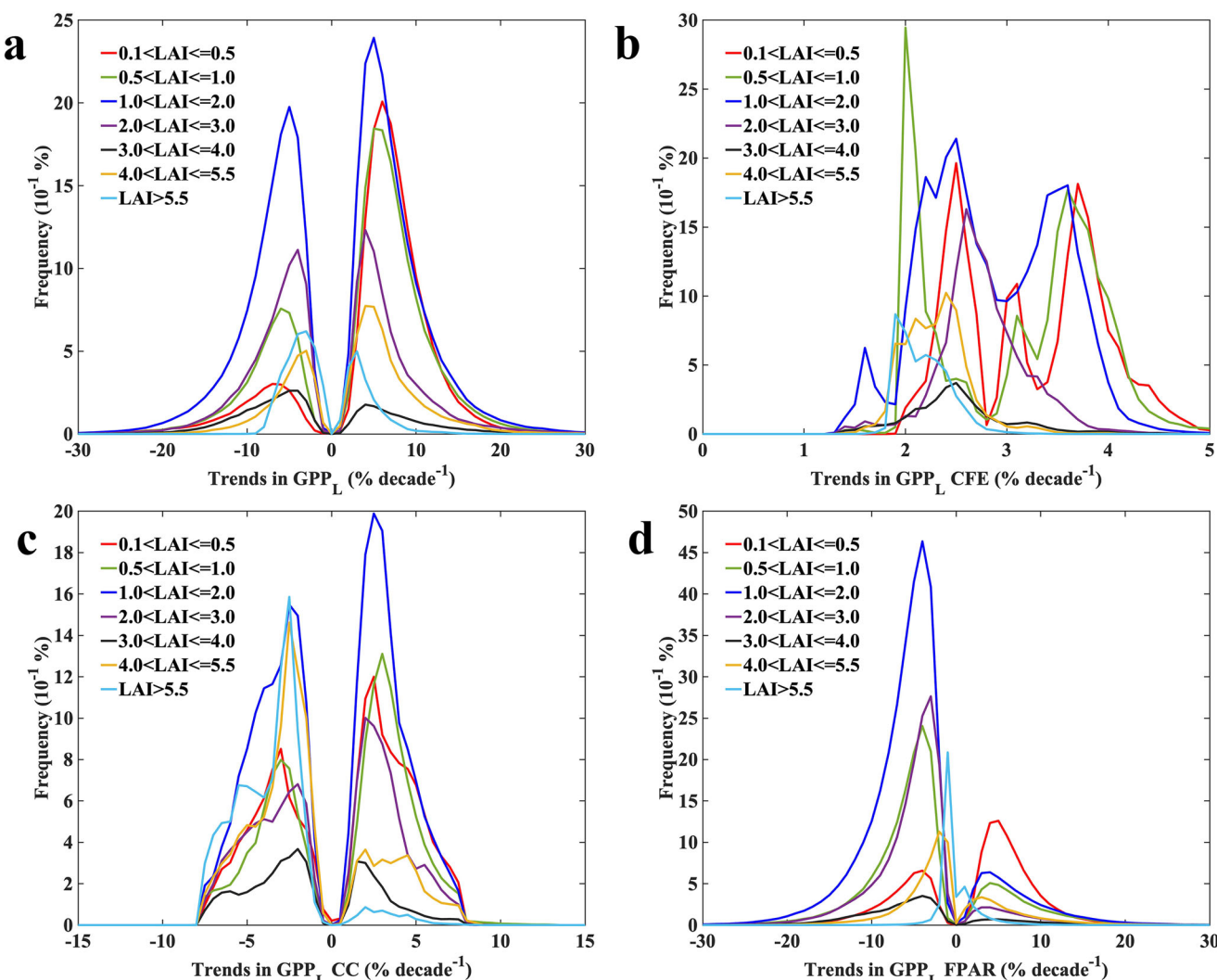


Fig. 2 | Distribution of leaf scale gross primary production (GPP_L) trends in different intervals of growing season average leaf area index (LAI). **a** GPP_L trends in simulations with time-varying CO_2 concentration, climate and fraction of vegetation-absorbed photosynthetically active radiation (FPAR) during 2001–2021 period. **b** GPP_L trends due only to the CO_2 fertilization effect (CFE). **c** GPP_L trends

due only to time-varying climate. **d** GPP_L trends due only to time-varying FPAR. The simulations with production efficiency models (PEMs) are described in Methods §11. The growing season is defined as the period when daily GPP_C > 0 and daily LAI > 0.1.

which closely mirrors that of total bimodal distribution, but the net change is a GPP_L gain in vegetation with LAI < 3, and loss in more dense vegetation. As a result, the combined effect of atmospheric CO_2 increase is a higher gain in leaf assimilation rates in sparse to moderately dense vegetation ($4\% \text{ decade}^{-1}$) and none in tropical forests, where GPP_L gains due to CFE are offset by losses due to changes in climate.

Changes in vegetation structure and leaf area alter light environment in canopies^{21,48}. This effect is represented in PEMs through data of fraction of

vegetation-absorbed photosynthetically active radiation (FPAR; Methods §1). The observations capture contemporaneous and the integral of legacy effects on structure and leaf area from CO_2 concentration, climate, nutrient availability and human management¹³. The absolute magnitudes of FPAR effects are larger than the CO_2 effects (Fig. 2d vs. b). They are negative nearly everywhere (Fig. 2d), preventing the positive influence of the CFE from entirely offsetting the overall negative GPP_L distribution, with the exception of shrublands where they are net-positive. The LAI gains from greening⁶

(Supplementary Fig. 7b) translate to smaller FPAR gains because of the nonlinear LAI-FPAR relationship arising from increased self-shading in denser leaf canopies (Supplementary Fig. 8). Consequently, GPP_C trends are smaller than leaf area trends, and hence, losses in GPP_L . In sparsely vegetated shrublands, increases in LAI translate linearly to FPAR to result in GPP_L gains. Thus, the effect of light on leaf assimilation rates is to offset the gains from the fertilisation effect, and climate if any, in nearly all vegetation with the exception of those with $LAI < 1$, *i.e.*, the arid and semi-arid land covers of shrublands and grasslands (Fig. 2a and Table 1).

§3 Regional Divergence in Leaf Scale Photosynthetic Rates

Of particular interest are two large regions, the Sudano-Sahelian zone and adjoining savanna in Africa ($7 \times 10^6 \text{ km}^2$; “Sahel +” from hereon) and, China and India combined ($9.5 \times 10^6 \text{ km}^2$). Much of the population of over 3×10^9 people in these regions depends on the land for livelihood. Both display significant increases in leaf area (Supplementary Fig. 7b) and GPP_C (Fig. 1a). However, GPP_L gains are conspicuous only in the Sahel+ region (Fig. 1b). GPP_L losses in China and India similarly stand out. This striking contrast can be understood by the effects of CO_2 , climate and light on GPP_L .

The Sahel+ region consists of herbaceous vegetation of shrublands, grasslands and croplands to the north and savannas to the south ($LAI \sim 1.2$). It experienced a rebound in precipitation after severe droughts in the 1970s and early 1980s. The area has greatly greened since then^{44,45}, settling a debate in favor of climate and against land degradation from human activities^{50,51}. This positive climate effect on photosynthate production is further enhanced by the CO_2 fertilisation effect (CFE). The resulting GPP_C gain is greater than the LAI trend ($10.4 \text{ vs. } 6.9\% \text{ decade}^{-1}$ in Fig. 3a), which suggests that the negative FPAR effect is outmatched by the positive effects of fertilisation and climate (Fig. 3c). Thus, the region exhibits prominent gains in leaf assimilation rates ($7.4\% \text{ decade}^{-1}$). Similar arguments explain the positive GPP_L trends in semi-arid parts of USA, Argentina, etc. (Supplementary Fig. 9a, c).

China and India lead in greening (Supplementary Fig. 7b) due to expanding natural forests and afforestation in the case of China and agricultural intensification in both⁵. China has implemented programmes to conserve and expand forests with the goal of mitigating climate change, while enhancing carbon sequestration^{52,53}. Agricultural intensification^{54,55} in both countries is facilitated by heavy fertilizer use and irrigation combined with multiple cropping. Consequently, forests and croplands account for 50

and 19% of the net increase in leaf area of China, whereas croplands alone contribute 80% in the case of India. The large greening trends (Fig. 3b), however, did not enhance leaf assimilation rates because of diminished absorbed lights on per unit of leaf surfaces. In fact, the FPAR effect on GPP_L is sufficiently negative that it more than offsets the positive effects of CO_2 fertilisation and climate change (Fig. 3d), with resulting losses in leaf assimilation rates ($-5\% \text{ decade}^{-1}$; Fig. 3b). This is also true in the case of Brazil and northern Europe (Supplementary Fig. 9b, d).

Conclusions

To summarize, observations and models show a consistent picture of dynamics in canopy- and leaf-scale assimilation rates and leaf area. Nearly half the vegetated lands display changes, mostly an increase, in canopy scale gross primary production (GPP_C) during the 2001–2021 period. This can be traced to variations in the extent of photosynthesizing leaf area (LAI) only, assimilation rates per unit leaf area (GPP_L) only, or both. Increasing trends in GPP_L and LAI are seen only in the sparse vegetation of arid and semi-arid climes, the Sahel and adjoining zone being a prime example. Here, the positive trends are sustained through the CFE, higher efficiency of water use and conducive light regime. Nearly everywhere else, the negative impacts of climate and/or FPAR effects attributable to greening dominate, as in the case of China and India. Here, the residual GPP_C gains are attributable to large LAI increases from intensive human land management. This largely explains the mis-match between greening and GPP changes. It also argues against conventional thinking the global greening will lead to more carbon sequestration. Earth system models project a saturation of GPP_L in all scenarios (Supplementary Fig. 10), but surprisingly no declines even in an atmosphere of over 1000 ppm of CO_2 concentration. Nevertheless, the current positive GPP_L trends and the potential for carbon sequestration¹⁷ highlight the need for conservation and sustainable use of arid and semi-arid lands.

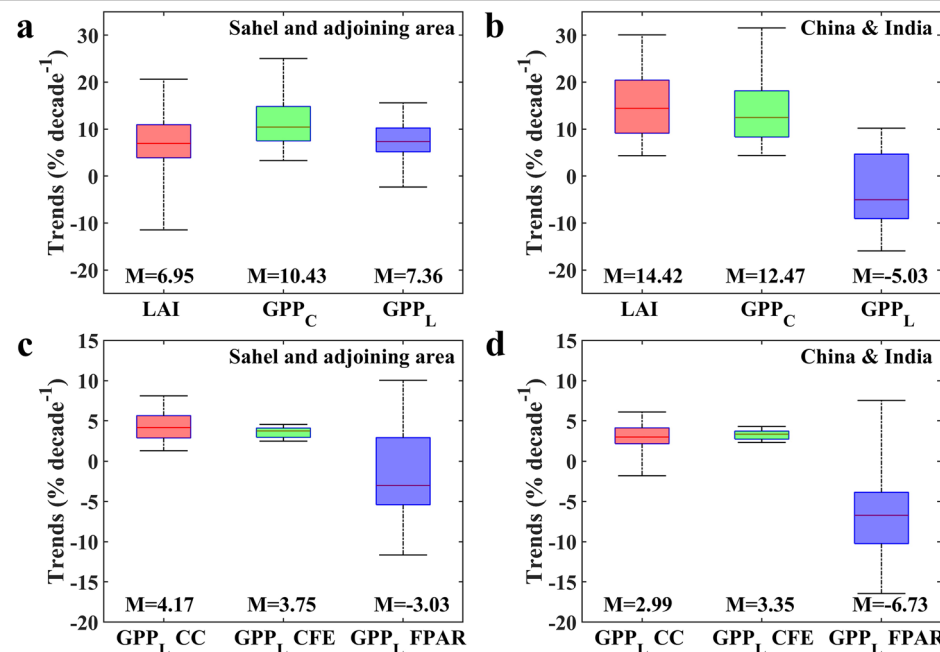
Methods

§1 Production Efficiency Models (PEMs)

This study included two of the most widely-used PEMs (PEMs 1 and 2 below) in addition to a more recently developed generalized PEM formulation (PEM3) to estimate the Gross Primary Production of vegetation canopies (GPP_C), globally at daily time scale for the period 2001 to 2021. These models represent the current state-of-the-art for modeling GPP_C

Fig. 3 | Comparison of trends in the Sahel and adjoining area and in China and India combined.

The Sahelian region is a rectangular area spanning 4.35° N to 15° N and 17.5° W to 51.5° E showing prominent gains in GPP_L (see Fig. 1b). a, b Trends in growing season average leaf area index (LAI), gross primary production at canopy scale (GPP_C) and leaf scale (GPP_L). c, d Trends in GPP_L due only to CO_2 (GPP_L CFE), climate change (GPP_L CC) and fraction of vegetation-absorbed photosynthetically active radiation (GPP_L FPAR). The box plots show the distribution of statistically significant trends (Mann-Kendall test, $P \leq 0.1$). The maximum and minimum values of the colored boxes represent the 25th and 75th percentiles, respectively, and the whiskers represent the 5th and 95th percentiles. The red line represents the median (M) trend. The growing season is defined as the period when $GPP_C > 0$ and daily LAI > 0.1 .



based on light use efficiency while accounting for the effects of temperature, vapour pressure deficit (VPD) and atmospheric CO₂. The models have the advantage of being simple while capturing tendencies seen in observations. They suffer from some well-known limitations, *viz.*, idealizing the canopy as one big leaf, highly parameterised representation of processes, etc.

PEM1. The model used for generating GPP_C product by the MODIS program⁵⁶ is modified to include the CO₂ fertilization effect^{13,57}. GPP_C (g C m⁻² day⁻¹) is calculated as

$$GPP_C^{M1} = LUE_{opt}^{M1} \times PAR \times FPAR \times f_{TMIN}^{M1} \times f_{VPD}^{M1} \times f(CO2) \quad (1)$$

where LUE_{opt}^{M1} is the optimal light use efficiency (g C MJ⁻¹), PAR is the incident photosynthetically active radiation (MJ m⁻² day⁻¹), FPAR is the fraction of vegetation absorbed PAR, f_{VPD}^{M1} is the water stress scalar (VPD) and f_{TMIN}^{M1} is the temperature (daily minimum) stress scalar. The CO₂ fertilization effect [f(CO₂)] is modelled by a relative value of C_s (current year, C_s^t) compared to a baseline period⁵⁷ (year 2001, C_s^{base}) as (C_s is similar to PEM2 below)

$$f(CO_2) = \frac{C_s^t}{C_s^{base}} \quad (2)$$

PEM2. GPP_C is calculated using the EC-LUE model⁵⁷ as

$$GPP_C^{M2} = LUE_{opt}^{M2} \times PAR \times FPAR \times C_s \times \min(f_T^{M2}, f_{VPD}^{M2}) \quad (3)$$

$$C_s = \frac{C_i - \Gamma^*}{C_i + 2\Gamma^*} \quad (4)$$

$$C_i = C_a \times \chi \quad (5)$$

where C_s is the effect of atmospheric CO₂ concentration on GPP_C^{35,37}. Γ^* is the CO₂ compensation point in the absence of dark respiration (ppm) and C_i is the CO₂ concentration in the intercellular air spaces of the leaf (ppm), which is the product of the atmospheric CO₂ concentration (C_a) and the ratio of internal to ambient CO₂ in the leaf (χ)^{8,58}. χ is calculated by

$$\chi = \frac{\Upsilon}{\Upsilon + \sqrt{VPD}} \quad (6)$$

$$\Upsilon = \sqrt{\frac{356.51 \times K}{1.6 \times \eta^*}} \quad (7)$$

$$K = K_c \times \left(1 + \frac{P_o}{K_o}\right) \quad (8)$$

$$K_c = 39.97 \times e^{\frac{79.43 \times (T_a - 298.15)}{298.15 \times R \times T_a}} \quad (9)$$

$$K_o = 27480 \times e^{\frac{36.38 \times (T_a - 298.15)}{298.15 \times R \times T_a}} \quad (10)$$

where K_c (Pa) and K_o (Pa) are the Michaelis-Menten coefficient of Rubisco for carboxylation and oxygenation, respectively⁸. P_o is the partial pressure of O₂ (Pa). R is the molar gas constant (8.314 J mol⁻¹ K⁻¹), T_a is air temperature, and η^* is the viscosity of water as a function of air temperature relative to its value at 25°C⁵⁹.

PEM3. The Max Planck Institute for Biogeochemistry (MPI-BGC) model⁶⁰ includes the effects of temperature, VPD, atmospheric CO₂ concentration, soil moisture (W), light intensity (L), and cloudiness

through an index (CI) on GPP_C. It evaluates GPP_C as

$$GPP_C^{M3} = LUE_{opt}^{M3} \times PAR \times FPAR \times f_T^{M3} \times f_W^{M3} \times f_{VPD,CO2}^{M3} \times f_L^{M3} \times f_{CI}^{M3} \quad (11)$$

$$f_{VPD,CO2}^{M3} = \left(e^{k \times \left(\frac{C_{a0}}{C_a} \right)^{C_k} \times VPD} \right) \times \left(1 + \frac{C_a - C_{a0}}{C_a - C_{a0} + c_m} \right) \quad (12)$$

Where k is the sensitivity to VPD changes, C_{a0} is the minimum optimal atmospheric CO₂ concentration, C_a is the atmospheric CO₂ concentration, C_k is the sensitivity to atmospheric CO₂ concentration changes, and c_m is the CO₂ fertilization intensity indicator⁶¹.

§2 input data for PEMs

Two climate data sets are used to force the PEMs – (1) GMAO MERRA-2 and (2) ECMWF ERA-5. Additional climate data required by PEM3 are obtained from GLDAS NOAH-2.1 (2001–2021). The climate data together with sensor-independent (SI) FPAR data⁷ are harmonised to daily and 0.05° resolutions to calculate GPP_C with the three PEMs. Daily CO₂ data from NOAA were used to model the fertilisation effect. The variable LUE in PEMs is land cover dependent, hence the MODIS landcover product⁶² is used to identify the landcover in each pixel. The rest of the variables are pixel dependent. All data are publicly available (see “Data Availability” statement).

§3 Estimation of Optimal LUE

Optimal values of light use efficiency (LUE_{opt}) for the 11 land covers are estimated iteratively and separately for the three PEMs using annual GPP_C estimates based on the average of the night-time (GPP_REF_NT_VUT) and day-time (GPP_REF_DT_VUT) partitioning approaches from the FLUX-NET2015 data set⁶³. The number of GPP_C estimates for each land cover varies depending on the number of sites belonging to that land cover and the number of years for which estimates are available (Supplementary Table S1). The optimisation is done iteratively as follows.

Step 1: Model GPP_C values corresponding to half the randomly selected GPP_C estimates are calculated by assuming LUE = 1 and using GMAO climate and SI FPAR data. Step 2: An estimate of LUE_{opt} is evaluated by linearly regressing modelled GPP_C against measured GPP_C. Step 3: Model GPP_C values corresponding to the other half of GPP_C estimates are calculated using LUE_{opt} estimated in Step 2. Step 4: The RMSE is calculated by regressing the modelled GPP_C values in Step 3 against the corresponding observed GPP_C values. Steps 1 to 4 are repeated 10,000 times to obtain 10,000 values of LUE_{opt} and corresponding RMSE. LUE_{opt} values corresponding to the lowest 9,500 RMSE values are averaged to obtain LUE_{opt}. This process is repeated separately for each landcover and for the three models – the resulting LUE_{opt} values are given in Supplementary Table S2.

A comparison of modelled and observations-based GPP_C values before and after optimisation is shown in Supplementary Fig. 1. The optimisation procedure improved performance of PEM1 and 2, but not PEM3 for the following reason. The original PEM3 contained parameters that varied at the 0.05° pixel-scale. This version agrees well with flux tower based GPP_C estimates as the parameters were tuned to those estimates. It however results in global GPP_C values nearly twice the other models and those reported in literature. When PEM3 is reformulated in terms of landcovers, the agreement with tower estimates degrades (Supplementary Fig. 1) but the geographical patterns and global totals match those of PEM1 and 2 (not shown for brevity).

§4 Evaluations of PEMs

The performance of PEMs is evaluated through comparisons with data from the AmeriFlux estimates. These (Supplementary Table S3) are different than the FLUXNET2015 estimates used to optimise the LUE variable of the three PEMs (§3). GPP_C values from the three PEMs compare satisfactorily (R² > 0.54 and RMSE < 483.64 g C m⁻² yr⁻¹) with tower estimates

(Supplementary Fig. 2). These results are similar to those in the literature regarding the performance of PEMs in general^{64–67}.

§5 Comparison of GPPC between PEMs

Modelled annual GPP_C from the three PEMs forced with two climate data sets varies between 120 and 135 Pg C yr⁻¹ (Supplementary Table S4). The agreement between the three PEMs at 445 BELMANIP2.1 test sites⁶⁸ is good (Supplementary Fig. 3; $R^2 > 0.90$ and RMSE between 251 to 327 g C m⁻² yr⁻¹). Average annual GPP_C from this ensemble of three PEMs forced with two climate data sets is used throughout this article.

§6 Comparison of GPPC from PEMs with Peer GPPC products

The modelled ensemble average GPP_C (three PEMs and two climate forcings) is compared to four other published global-scale GPP_C data sets for consistency. These GPP_C data sets are independent of one another. The GOSIF GPP_C product is generated using relationships between satellite-measured Solar-Induced chlorophyll Fluorescence (SIF) and observed GPP_C ²³. The Random Forest (RF) GPP_C product is generated from a combination of a nested machine learning model and a theoretical photosynthesis model²⁶. The FLUXCOM and X-BASE FLUXCOM GPP_C products are a result of upscaling approaches based on machine learning methods that integrate flux tower estimates, satellite remote sensing, and meteorological data^{27,28}. The modelled PEM ensemble average GPP_C compares well to all four published data sets (Supplementary Fig. 4 and Supplementary Table S5). The comparisons at BELMANIP2.1 test sites indicate $R^2 > 0.91$ and RMSE between 224 to 277 g C m⁻² yr⁻¹ (Supplementary Fig. 5).

§7 Dynamic Global Vegetation Models (DGVMs)

A project comprising of an international ensemble of DGVMs known as the “Trends and drivers of the regional scale terrestrial sources and sinks of carbon dioxide” (TRENDY) quantifies land biophysical exchange processes and biogeochemistry cycles²⁴. Output at monthly resolution from TRENDYv12 simulations with varying land use change, climate, and CO₂ (S3) of the following 18 models is used in this article: CABLE-POP, CLASSIC, CLM5.0, DLEM, E3SM, EDv3, IBIS, ISBA-CTRP, JSBACH, JULES, LPJ-GUESS, LPJmL, LPX-Bern, OCN, ORCHIDEEv3, SDGVM, VISIT, and YIBs.

§8 CMIP6 Earth System Models

The sixth Coupled Model Intercomparison Project (CMIP6) is the latest to use a suite of Earth System Models (ESMs) to produce global simulations of the past, current, and future climate^{4,25}. Monthly output from CMIP6 simulations from the following seven ESMs are used in our analyses: ACCESS-ESM1-5, CanESM5, CanESM5-CanOE, EC-Earth3-CC, GFDL-ESM4, MPI-ESM1-2-LR, and NorESM2-LM. Four of these models that included an interactive terrestrial Nitrogen cycle demonstrated improved GPP_C simulations (ACCESS-ESM1-5, EC-Earth3-CC, MPI-ESM1-2-LR, and NorESM2-LM)⁶¹. All ESMs included dynamic vegetation models. These DGVMs are a subset of the TRENDY DGVMs described in §7. The representation and evaluation of the terrestrial carbon cycle in these models is described in Gier et al.⁶⁹. Simulated GPP_C and LAI from historical (2001 to 2014) and projection (2015–2100) periods are analysed in this study. The latter are for three emission scenarios – Shared Socio-economic Pathways (SSPs) 2-4.5, 3-7.0 and 5-8.5.

§9 Leaf Area Index Data

Two publicly available LAI data sets are used in this study: a sensor independent LAI data set⁷ and the GLASS LAI data set^{39,42}. The data sets are derived independently from MODIS and other satellite-based sensors with algorithms that have been well tested over the past three decades^{70–73}. The two LAI datasets exhibited similar spatial and trend distributions, showing no significant discrepancies in most regions^{7,39,42,72}. The LAI data are not used in the calculation of GPP_C reported in this article. LAI values from the two data sets are averaged and interpolated from 8-day to daily resolution.

This mean LAI data set was used in this study to avoid large uncertainties that would arise if SI LAI/FPAR were directly used as input for GPP_L calculations.

§10 Calculation of GPP_L

Leaf photosynthetic carbon assimilation rate, GPP_L (g C m⁻² leaf area day⁻¹), is calculated as the ratio of daily GPP_C to daily LAI. In the case of PEMs, GPP_L is calculated with the ensemble average GPP_C from the three models (§1) forced with two climate data sets (§2) and satellite-based LAI (§9). Theoretically, the non-linear LAI-FPAR relationship has varying effects on GPP_L across sparse and dense canopies, primarily by altering light distribution on leaves due to changes in vegetation structure^{21,22}. Therefore, this study will clarify the light-related effects on GPP_L changes based on this non-linear LAI-FPAR relationship. In the case of GOSIF, GPP_L is calculated with GPP_C from observations-based GOSIF data set²³ and satellite-based LAI (§9). In the case of TRENDY models (§7) and CMIP6 ESMs (§8), GPP_L is calculated with each model simulated GPP_C and LAI. These SIF-based and model-based GPP_L estimates can be used to independently corroborate the accuracy of GPP_L obtained from the PEMs.

§11 Sensitivity Analyses with PEMs

Sensitivity simulations are performed with PEMs following the TRENDY protocol³ to quantify the contributions of the CO₂ fertilisation effect (CFE), climate change and FPAR on gross primary production at canopy (GPP_C) and leaf scale (GPP_L). The CFE is quantified through simulation S1 by using constant climate (2001–2003 average), FPAR, and landcover from year 2001 and time-varying observed CO₂ concentration for the period 2001–2021. The climate effect is quantified as the difference between simulations S2 and S1, where S2 is performed with FPAR and landcover from year 2001 and time-varying observed CO₂ concentration and climate for the period 2001–2021. Finally, the effect of FPAR is quantified as the difference between simulations S3 and S2, where S3 is performed with time-varying observed CO₂ concentration, climate, FPAR and landcover for the period 2001–2021. All simulations are performed with the three PEMs (§1) and two climate data sets (§2) and the ensemble average GPP_C is used in further analyses. GPP_L in simulations S1 and S2 is calculated as the ratio of GPP_C to LAI in year 2001 at the daily scale during the growing season ($GPP_C > 0$ and LAI > 0.1). It is calculated using time-varying LAI during 2001–2021 in simulation S3. Notably, land cover information in S3 changes only in conjunction with LAI/FPAR, and the FPAR effect implicitly incorporates land use/land cover changes. Thus, one limitation of this study is that the influence of land use/land cover changes in the PEM model cannot be directly calculated.

The coupled carbon-climate systems includes complicated linkages between various components and processes via feedbacks and lags^{14,74,75}. The more complex dynamic models, TRENDY DGVMs (§7) and CMIP6 ESMs (§8), include some but not all of the known linkages. Sensitivity simulations similar to those described above are available from TRENDY²⁴, however these are not used because of differences, relative to observations, in modelled LAI distribution across the entire vegetated area, both in magnitude and seasonal course. The PEMs have the advantage of incorporating measured data (CO₂, Climate and FPAR) while also being simple. These models capture the direct effects of these variables on primary production. Thus, the sensitivity simulations with PEMs serve the stated goal of understanding the observed spatial patterns of GPP_L to a first order.

Data availability

All data used to support the findings of this study are publicly available. They can be obtained as follows: PEM GPP data – doi.org/10.5281/zenodo.13989451; GMAO MERRA-2 data – gmao.gsfc.nasa.gov/reanalysis/MERRA-2; ECMWF ERA-5 data – cds.climate.copernicus.eu/cdsapp#!/dataset/reanalysis-era5-single-levels; GLDAS NOAH 2.1 data – disc.gsfc.nasa.gov/datasets?keywords=GLDAS; SI FPAR data – doi.org/10.5281/zenodo.8076540; FLUXNET2015 data – fluxnet.org/data/fluxnet2015-dataset/; AmeriFlux data – ameriflux.lbl.gov/ data/download-

data/; GOSIF GPP data – data.globalecology.unh.edu/data/GOSIF_v2/; RF GPP data – zenodo.org/records/10018475; FLUXCOM GPP data – fluxcom.org/; FLUXCOM-X GPP data – meta.icos-cp.eu/collections/AYj7-IwcdCLnBXJDoscxQZou; TRENDY are available on request from TRENDY coordinator S. Sitch (s.a.sitch@exeter.ac.uk); CMIP6 simulations – aims2.llnl.gov/search; SI LAI data – <https://doi.org/10.5281/zenodo.8076540>; GLASS LAI data – www.glass.umd.edu/index.html; CO₂ concentration data – gml.noaa.gov/ccgg/trends/; Aridity index – figshare.com/articles/dataset/Global_Aridity_Index_and_Potential_Evapotranspiration_ET0_Climate_Database_v2/7504448 MCD12Q1 – ladsweb.modaps.eosdis.nasa.gov/missions-and-measurements/products/MCD12Q1.

Received: 26 March 2025; Accepted: 10 December 2025;

Published online: 21 December 2025

References

- Wang, H. et al. Towards a universal model for carbon dioxide uptake by plants. *Nat. Plants* **3**, 734–741 (2017).
- Chen, C. et al. CO₂ fertilization of terrestrial photosynthesis inferred from site to global scales. *Proc. Natl. Acad. Sci. USA* **119**, e2115627119 (2022).
- Ruehr, S. et al. Evidence and attribution of the enhanced land carbon sink. *Nat. Rev. Earth Environ.* **4**, 518–534 (2023).
- Myndeni, R. B. et al. Global products of vegetation leaf area and fraction absorbed PAR from one year of MODIS data. *Remote Sens. Environ.* **83**, 214–231 (2002).
- Chen, C. et al. China and India lead in greening of the world through land-use management. *Nat. Sustain.* **2**, 122–129 (2019).
- Piao, S. et al. Characteristics, drivers and feedbacks of global greening. *Nat. Rev. Earth Environ.* **1**, 14–27 (2020).
- Pu, J. et al. Sensor-independent LAI/FPAR CDR: reconstructing a global sensor-independent climate data record of MODIS and VIIRS LAI/FPAR from 2000 to 2022. *Earth Syst. Sci. Data* **16**, 15–34 (2024).
- Keenan, T. F. et al. Recent pause in the growth rate of atmospheric CO₂ due to enhanced terrestrial carbon uptake. *Nat Communications* **7**, 13428 (2016).
- Keenan, T. F. & Riley, W. J. Greening of the land surface in the world's cold regions consistent with recent warming. *Nat. Clim. Chang.* **8**, 825–828 (2018).
- Pugh, T. A. et al. Important role of forest disturbances in the global biomass turnover and carbon sinks. *Nat. Geosci.* **12**, 730–735 (2019).
- Haverd, V. et al. Higher than expected CO₂ fertilization inferred from leaf to global observations. *Glob. Chang. Biol.* **26**, 2390–2402 (2020).
- Walker, A. P. et al. Integrating the evidence for a terrestrial carbon sink caused by increasing atmospheric CO₂. *N. Phytol.* **5**, 2413–2445 (2020).
- Keenan, T. F. et al. A constraint on historic growth in global photosynthesis due to rising CO₂. *Nat. Clim. Chang.* **13**, 1376–1381 (2023).
- Winkler, A. J. et al. Carbon system state determines warming potential of emissions. *PLoS ONE* **19**, e0306128 (2024).
- Zhu, Z. et al. Greening of the Earth and its drivers. *Nat. Clim. Chang.* **6**, 791–795 (2016).
- Wang, S. et al. Drylands contribute disproportionately to observed global productivity increases. *Science Bulletin* **68**, 224–232 (2023).
- Poulter, B. et al. Contribution of semi-arid ecosystems to interannual variability of the global carbon cycle. *Nature* **509**, 600 (2014).
- Xu, L. et al. Widespread decline in greenness of Amazonian vegetation due to the 2010 drought. *Geophys. Res. Lett.* **38**, L07402 (2011).
- Doughty, C. E. et al. Drought impact on forest carbon dynamics and fluxes in Amazonia. *Nature* **519**, 78–82 (2015).
- Yang, J. et al. Amazon drought and forest response: largely reduced forest photosynthesis but slightly increased canopy greenness during the extreme drought of 2015/2016. *Glob. Change Biol.* **24**, 1919–1934 (2018).
- Thornley, J. H. Instantaneous canopy photosynthesis: analytical expressions for sun and shade leaves based on exponential light decay down the canopy and an acclimated non-rectangular hyperbola for leaf photosynthesis. *Ann. Bot.* **89**, 451–458 (2002).
- Brodersen, C. R. & Vogelmann, T. C. Do changes in light direction affect absorption profiles in leaves? *Funct. Plant Biol.* **37**, 403–412 (2010).
- Li, X. & Xiao, J. Mapping photosynthesis solely from solar-induced chlorophyll fluorescence: A global, fine-resolution dataset of gross primary production derived from OCO-2. *Remote Sens. Environ.* **11**, 2563 (2019).
- Stich, S. et al. Trends and Drivers of Terrestrial Sources and Sinks of Carbon Dioxide: An Overview of the TRENDY Project. *Glob. Biogeochem. Cycles* **38**, e2024GB008102 (2024).
- Eyring, V. et al. Overview of the Coupled Model Intercomparison Project Phase 6 (CMIP6) experimental design and organization. *Geosci. Model Dev.* **9**, 1937–1958 (2016).
- Chen, Y. et al. The direct and indirect effects of the environmental factors on global terrestrial gross primary productivity over the past four decades. *Environ. Res. Lett.* **19**, 014052 (2023).
- Jung, M. et al. The FLUXCOM ensemble of global land-atmosphere energy fluxes. *Sci Data* **6**, 74 (2019).
- Nelson, J. A. et al. X-BASE: the first terrestrial carbon and water flux products from an extended data-driven scaling framework, FLUXCOM-X. *Biogeosciences* **21**, 5079–5115 (2024).
- Cai, W. & Prentice, I. C. Recent trends in gross primary production and their drivers: analysis and modelling at flux-site and global scales. *Environ. Res. Lett.* **15**, 124050 (2020).
- O'Sullivan, M. et al. Climate-driven variability and trends in plant productivity over recent decades based on three global products. *Glob. Biogeochem. Cyc.* **34**, e2020GB006613 (2020).
- Myndeni, R. B. et al. Increased plant growth in the northern high latitudes from 1981 to 1991. *Nature* **386**, 698–702 (1997).
- Zhou, L. et al. Variations in northern vegetation activity inferred from satellite data of vegetation index during 1981 to 1999. *J. Geophys. Res. Atmos.* **106**, 20069–20083 (2001).
- Park, T. et al. Changes in growing season duration and productivity of northern vegetation inferred from long-term remote sensing data. *Environ. Res. Lett.* **11**, 084001 (2016).
- Winkler, A. J. et al. Slowdown of the greening trend in natural vegetation with further rise in atmospheric CO₂. *Biogeosciences* **18**, 4985–5010 (2021).
- Farquhar, G. D., von Caemmerer, S. & Berry, J. A. A biochemical model of photosynthetic CO₂ assimilation in leaves of C₃ species. *Planta* **149**, 78–90 (1980).
- Gutschick, V. P. Photosynthesis model for C₃ leaves incorporating CO₂ transport, propagation of radiation, and biochemistry. 1. Kinetics and their parameterization. *Photosynthetica* **18**, 549–568 (1984).
- Collatz, G. J. et al. Physiological and environmental-regulation of stomatal conductance, photosynthesis and transpiration - a model that includes a laminar boundary-layer. *Agric. For. Meteorol.* **54**, 107–136 (1991).
- Stocker, B. D. et al. P-model v1.0: an optimality-based light use efficiency model for simulating ecosystem gross primary production. *Geosci. Model Dev.* **13**, 1545–1581 (2020).
- Liang, S. et al. The global land surface satellite (GLASS) product suite. *Bull. Am. Meteorol. Soc.* **102**, E323–E337 (2021).
- Yan, K. et al. HiQ LAI: A high-quality reprocessed MODIS leaf area index dataset with better spatiotemporal consistency from 2000 to 2002. *Earth Syst. Sci. Data* **16**, 1601–1622 (2024).
- Cao, S. et al. Spatiotemporally consistent global dataset of the GIMMS leaf area index (GIMMS LAI4g) from 1982 to 2020. *Earth Syst. Sci. Data* **15**, 4877–4899 (2023).
- Ma, H. & Liang, S. Development of the GLASS 250-m leaf area index product (version 6) from MODIS data using the bidirectional LSTM deep learning model. *Remote Sens. Environ.* **273**, 112985 (2022).

43. Wei, F. et al. Divergent trends of ecosystem-scale photosynthetic efficiency between arid and humid lands across the globe. *Glob. Ecol. Biogeogr.* **31**, 1824–1837 (2022).

44. Dardel, C. et al. Re-greening Sahel: 30 years of remote sensing data and field observations (Mali, Niger). *Remote Sens. Environ.* **140**, 350–364 (2014).

45. Brandt, M. et al. Ground- and satellite-based evidence of the biophysical mechanisms behind the greening Sahel. *Glob. Change Biol.* **21**, 1610–1620 (2015).

46. Yuan, W. et al. Increased atmospheric vapor pressure deficit reduces global vegetation growth. *Sci. Adv.* **5**, eaax1396 (2019).

47. Faticchi, S. et al. Partitioning direct and indirect effects reveals the response of water-limited ecosystems to elevated CO₂. *Proc. Natl Acad. Sci.* **113**, 12757–12762 (2016).

48. Knyazikhin, Y. et al. Synergistic algorithm for estimating vegetation canopy leaf area index and fraction of absorbed photosynthetically active radiation from MODIS and MISR data. *J. Geophys. Res.* **103**, 32257–32276 (1998).

49. Norby, R. J. et al. Forest response to elevated CO₂ is conserved across a broad range of productivity. *Proc. Natl Acad. Sci. USA* **102**, 18052–18056 (2005).

50. Kaptu  , A. T., Prihodko, L. & Hanan, N. P. On regreening and degradation in Sahelian watersheds. *Proc. Natl Acad. Sci. USA* **112**, 12133–12138 (2015).

51. Min, J. et al. Understanding spatial patterns in the drivers of greenness trends in the Sahel-Sudano-Guinean region. *Big Earth Data* **7**, 298–317 (2023).

52. Zhang, Y. et al. Multiple afforestation programs accelerate the greenness in the ‘Three North’ region of China from 1982 to 2013. *Ecol. Indic.* **61**, 404–412 (2016).

53. Lu, F. et al. Effects of national ecological restoration projects on carbon sequestration in China from 2001 to 2010. *Proc. Natl Acad. Sci. USA* **115**, 4039–4044 (2018).

54. Ray, D. K. & Foley, J. A. Increasing global crop harvest frequency: recent trends and future directions. *Environ. Res. Lett.* **8**, 044041 (2013).

55. Mueller, N. D. et al. Closing yield gaps through nutrient and water management. *Nature* **490**, 254–257 (2012).

56. Running, S. W. & Zhao, M. Daily GPP and Annual NPP (MOD17A2/A3) Products NASA Earth Observing System MODIS Land Algorithm—User’s Guide V3. 28 (MODIS Land Team, 2015).

57. Yuan, W. et al. Deriving a light use efficiency model from eddy covariance flux data for predicting daily gross primary production across biomes. *Agric. For. Meteorol.* **143**, 189–207 (2007).

58. Prentice, I. C. et al. Balancing the costs of carbon gain and water transport: testing a new theoretical framework for plant functional ecology. *Ecol. Lett.* **17**, 82–91 (2014).

59. Korson, L., Drost-hansen, W. & Millero, F. J. Viscosity of water various temperatures. *J. Phys. Chem.* **73**, 34–39 (1969).

60. Bao, S. et al. Environment-sensitivity functions for gross primary productivity in light use efficiency models. *Agric. For. Meteorol.* **312**, 108708 (2022).

61. Kalliokoski, T. et al. Decomposing sources of uncertainty in climate change projections of boreal forest primary production. *Agric. For. Meteorol.* **262**, 192–205 (2018).

62. Sulla-Menashe, D. & Friedl, M. A. User Guide to Collection 6 MODIS Land Cover (MCD12Q1 and MCD12C1) Product (USGS, 2018).

63. Pastorello, G. et al. The FLUXNET2015 dataset and the ONEFlux processing pipeline for eddy covariance data. *Sci. Data* **7**, 225 (2020).

64. Zheng, Y. et al. Improved estimate of global gross primary production for reproducing its long-term variation, 1982–2017. *Earth Syst. Sci. Data* **12**, 2725–2746 (2020).

65. Wang, L. et al. Evaluation of the latest MODIS GPP products across multiple biomes using global eddy covariance flux data. *Remote Sens.* **9**, 418 (2017).

66. Zhu, W., Zhao, C. & Xie, Z. An end-to-end satellite-based GPP estimation model devoid of meteorological and land cover data. *Agric. For. Meteorol.* **331**, 109337 (2023).

67. Bai, Y. et al. Different satellite products revealing variable trends in global gross primary production. *J. Geophys. Res.* **128**, e2022JG006918 (2023).

68. Baret, F. et al. Evaluation of the representativeness of networks of sites for the global validation and intercomparison of land biophysical products: proposition of the CEOS-BELMANIP. *IEEE Trans. Geosci. Remote Sens.* **44**, 1794–1803 (2006).

69. Gier, B. K. et al. Representation of the terrestrial carbon cycle in CMIP6. *Biogeosciences* **21**, 5321–5360 (2024).

70. Yan, K. et al. Evaluation of MODIS LAI/FPAR Product Collection 6. Part 1: Consistency and Improvements. *Remote Sens.* **8**, 350 (2016).

71. Yan, K. et al. Evaluation of MODIS LAI/FPAR Product Collection 6. Part 2: Validation and Intercomparison. *Remote Sens.* **8**, 460 (2016).

72. Jin, H. et al. Intercomparison and validation of MODIS and GLASS leaf area index (LAI) products over mountain areas: A case study in southwestern China. *Int. J. Appl. Earth Obs. Geoinf.* **55**, 52–67 (2017).

73. Zhang, X. et al. An insight into the internal consistency of MODIS global leaf area index products. *IEEE Trans. Geosci.* **62**, 1–16 (2024).

74. Arneth, A. et al. Terrestrial biogeochemical feedbacks in the climate system. *Nat. Geosci.* **3**, 525–532 (2010).

75. Heinze, C. et al. ESD reviews: climate feedbacks in the Earth system and prospects for their evaluation. *Earth Syst. Dyn.* **10**, 379–452 (2019).

Acknowledgements

The authors thank (1) S. Sitch and TRENDY participants for sharing their simulations output, (2) N. Carvalhais and S. Bao for help with PEM3 and (3) Colin Prentice and Trevor Keenan for comments on drafts of this manuscript. The research at BU was funded by NASA Earth Science Division.

Author contributions

J.P.: Conceptualization, Data curation, Formal analysis, Investigation, Methodology, Software, Validation, Visualization, Writing – review & editing. **Y.C.:** Conceptualization, Methodology, Validation. **A.W.:** Formal analysis, Investigation. **Z.Z.:** Formal analysis, Methodology. **C.C.:** Investigation, Supervision. **Y.K.:** Conceptualization, Methodology, Resources. **R.M.:** Conceptualization, Funding acquisition, Methodology, Project administration, Resources, Supervision, Writing – original draft, Writing – review & editing.

Competing interests

The authors declare no competing interests.

Additional information

Supplementary information The online version contains supplementary material available at <https://doi.org/10.1038/s43247-025-03121-3>.

Correspondence and requests for materials should be addressed to Jiabin Pu.

Peer review information *Communications Earth and Environment* thanks the anonymous reviewers for their contribution to the peer review of this work. Primary Handling Editors: Dushan Kumarathunge and Mengjie Wang. A peer review file is available.

Reprints and permissions information is available at <http://www.nature.com/reprints>

Publisher’s note Springer Nature remains neutral with regard to jurisdictional claims in published maps and institutional affiliations.

Open Access This article is licensed under a Creative Commons Attribution-NonCommercial-NoDerivatives 4.0 International License, which permits any non-commercial use, sharing, distribution and reproduction in any medium or format, as long as you give appropriate credit to the original author(s) and the source, provide a link to the Creative Commons licence, and indicate if you modified the licensed material. You do not have permission under this licence to share adapted material derived from this article or parts of it. The images or other third party material in this article are included in the article's Creative Commons licence, unless indicated otherwise in a credit line to the material. If material is not included in the article's Creative Commons licence and your intended use is not permitted by statutory regulation or exceeds the permitted use, you will need to obtain permission directly from the copyright holder. To view a copy of this licence, visit <http://creativecommons.org/licenses/by-nc-nd/4.0/>.

© The Author(s) 2025